

Design of wide-angle selective absorbers/emitters with dielectric filled metallic photonic crystals for energy applications

Jeffrey B. Chou,^{1,*} Yi Xiang Yeng,^{2,3} Andrej Lenert,¹ Veronika Rinnerbauer,^{2,3} Ivan Celanovic,³ Marin Soljačić,^{2,3,4} Evelyn N. Wang,¹ and Sang-Gook Kim¹

¹Department of Mechanical Engineering, Massachusetts Institute of Technology, 77 Massachusetts Avenue, Cambridge, Massachusetts, USA

²Research Laboratory of Electronics, Massachusetts Institute of Technology, 77 Massachusetts Avenue, Cambridge, Massachusetts, USA

³Institute of Soldier Nanotechnologies, Massachusetts Institute of Technology, 77 Massachusetts Avenue, Cambridge, Massachusetts, USA

⁴Department of Physics, Massachusetts Institute of Technology, 77 Massachusetts Avenue, Cambridge, Massachusetts, USA
[*jeffchou@mit.edu](mailto:jeffchou@mit.edu)

Abstract: The design and simulation of a wide angle, spectrally selective absorber/emitter metallic photonic crystal (MPhC) is presented. By using dielectric filled cavities, the angular, spectrally selective absorption/emission of the MPhC is dramatically enhanced over an air filled design by minimizing diffraction losses. Theoretical analysis is performed and verified via rigorous coupled wave analysis (RCWA) based simulations. An efficiency comparison of the dielectric filled designs for solar thermophotovoltaic applications is performed for the absorber and emitter which yields a 7% and 15.7% efficiency improvement, respectively, compared to air filled designs. The converted power output density is also improved by 33.5%.

©2013 Optical Society of America

OCIS codes: (050.6624) Subwavelength structures; (050.1940) Diffraction; (230.5298) Photonic crystals; (290.6815) Thermal emission; (300.1030) Absorption; (300.2140) Emission.

References and links

1. W. R. Chan, P. Bermel, R. C. N. Pilawa-Podgurski, C. H. Marton, K. F. Jensen, J. J. Senkevich, J. D. Joannopoulos, M. Soljačić, and I. Celanovic, "Toward high-energy-density, high-efficiency, and moderate-temperature chip-scale thermophotovoltaics," *Proc. Natl. Acad. Sci. U.S.A.* **110**(14), 5309–5314 (2013).
2. W. Yang, S. Chou, C. Shu, H. Xue, Z. W. Li, D. T. Li, and J. F. Pan, "Microscale combustion research for application to micro thermophotovoltaic systems," *Energy Convers. Manage.* **44**(16), 2625–2634 (2003).
3. L. M. Fraas, J. E. Avery, and H. X. Huang, "Thermophotovoltaic furnace-generator for the home using low bandgap GaSb cells," *Semicond. Sci. Technol.* **18**(5), S247–S253 (2003).
4. H. Yugami, H. Sai, K. Nakamura, N. Nakagawa, and H. Ohtsubo, "Solar thermophotovoltaic using Al₂O₃/Er₃Al₅O₁₂ eutectic composite selective emitter," in *Conference Record of the Twenty-Eighth IEEE Photovoltaic Specialists Conference*, pp. 1214–1217 (2000).
5. K. W. Stone, N. S. Fatemi, and L. M. Garverick, "Operation and component testing of a solar thermophotovoltaic power system," *Conference Record of the Twenty-Fifth IEEE Photovoltaic Specialists Conference* 1421–1424 (1996).
6. V. M. Andreev, V. A. Grilikhes, V. P. Khvostikov, O. A. Khvostikova, V. D. Rumyantsev, N. A. Sadchikov, and M. Z. Shvarts, "Concentrator PV modules and solar cells for TPV systems," *Sol. Energy Mater. Sol. Cells* **84**(1–4), 3–17 (2004).
7. I. Celanovic, F. O'Sullivan, M. Ilak, J. Kassakian, and D. Perreault, "Design and optimization of one-dimensional photonic crystals for thermophotovoltaic applications," *Opt. Lett.* **29**(8), 863–865 (2004).
8. Y. X. Yeng, M. Ghebrebrhan, P. Bermel, W. R. Chan, J. D. Joannopoulos, M. Soljačić, and I. Celanovic, "Enabling high-temperature nanophotonics for energy applications," *Proc. Natl. Acad. Sci. U.S.A.* **109**(7), 2280–2285 (2012).

9. H. Sai, H. Yugami, Y. Kanamori, and K. Hane, "Solar selective absorbers based on two-dimensional W surface gratings with submicron periods for high-temperature photothermal conversion," *Sol. Energy Mater. Sol. Cells* **79**(1), 35–49 (2003).
10. D. Kirikae, Y. Suzuki, and N. Kasagi, "A silicon microcavity selective emitter with smooth surfaces for thermophotovoltaic power generation," *J. Micromech. Microeng.* **20**(10), 104006 (2010).
11. V. Rinnerbauer, S. Ndao, Y. Xiang Yeng, J. J. Senkevich, K. F. Jensen, J. D. Joannopoulos, M. Soljacic, I. Celanovic, and R. D. Geil, "Large-area fabrication of high aspect ratio tantalum photonic crystals for high-temperature selective emitters," *J. Vac. Sci. Technol. B* **31**(1), 011802 (2013).
12. S. Y. Lin, J. Moreno, and J. G. Fleming, "Three-dimensional photonic-crystal emitter for thermal photovoltaic power generation," *Appl. Phys. Lett.* **83**(2), 380–382 (2003).
13. C. Schlemmer, J. Aschaber, V. Boerner, and J. Luther, "Thermal stability of micro-structured selective tungsten emitters," *AIP Conf. Proc.* **653**(1), 164–173 (2003).
14. H.-J. Lee, K. Smyth, S. Bathurst, J. Chou, M. Ghebrebrhan, J. Joannopoulos, N. Saka, and S.-G. Kim, "Hafnia-plugged microcavities for thermal stability of selective emitters," *Appl. Phys. Lett.* **102**(24), 241904 (2013).
15. W.-C. Chen, M. Koirala, X. Liu, T. Tyler, K. G. West, C. M. Bingham, T. Starr, A. F. Starr, N. M. Jokerst, and W. J. Padilla, "Characterization of Surface Electromagnetic Waves and Scattering on Infrared Metamaterial Absorbers," eprint <http://arxiv.org/abs/1212.2868> (2012).
16. J. Hao, J. Wang, X. Liu, W. J. Padilla, L. Zhou, and M. Qiu, "High performance optical absorber based on a plasmonic metamaterial," *Appl. Phys. Lett.* **96**(25), 251104 (2010).
17. X. Liu, T. Tyler, T. Starr, A. F. Starr, N. M. Jokerst, and W. J. Padilla, "Taming the blackbody with infrared metamaterials as selective thermal emitters," *Phys. Rev. Lett.* **107**(4), 045901 (2011).
18. Y. Cui, K. H. Fung, J. Xu, H. Ma, Y. Jin, S. He, and N. X. Fang, "Ultrabroadband light absorption by a sawtooth anisotropic metamaterial slab," *Nano Lett.* **12**(3), 1443–1447 (2012).
19. E. Rephaeli and S. Fan, "Tungsten black absorber for solar light with wide angular operation range," *Appl. Phys. Lett.* **92**(21), 211107 (2008).
20. E. Rephaeli and S. Fan, "Absorber and emitter for solar thermo-photovoltaic systems to achieve efficiency exceeding the Shockley-Queisser limit," *Opt. Express* **17**(17), 15145–15159 (2009).
21. N. P. Sergeant, O. Pincon, M. Agrawal, and P. Peumans, "Design of wide-angle solar-selective absorbers using aperiodic metal-dielectric stacks," *Opt. Express* **17**(25), 22800–22812 (2009).
22. C. Wu, B. Neuner III, J. John, A. Milder, B. Zollars, S. Savoy, and G. Shvets, "Metamaterial-based integrated plasmonic absorber/emitter for solar thermo-photovoltaic systems," *J. Opt.* **14**(2), 024005 (2012).
23. J. Chou, K. Smyth, and S. Kim, "Low aspect ratio nanophotonic filled cavities with Q-matching for scalable thermophotovoltaic power conversion," presented at the 26th IEEE Photonics Conference, Bellevue Washington, 576–577, (2013).
24. J. D. Jackson, *Classical Electrodynamics Third Edition*, 3rd ed. (Wiley, 1998).
25. H. A. Haus, *Waves and Fields in Optoelectronics* (Prentice-Hall, 1984).
26. M. Ghebrebrhan, P. Bermel, Y. X. Yeng, I. Celanovic, M. Soljacic, and J. D. Joannopoulos, "Tailoring thermal emission via Q matching of photonic crystal resonances," *Phys. Rev.* **83**(3), 033810 (2011).
27. R. W. Wood, "Anomalous diffraction gratings," *Phys. Rev.* **48**(12), 928–936 (1935).
28. I. Celanovic, N. Jovanovic, and J. Kassakian, "Two-dimensional tungsten photonic crystals as selective thermal emitters," *Appl. Phys. Lett.* **92**(19), 193101 (2008).
29. V. Liu and S. Fan, "S4 : A free electromagnetic solver for layered periodic structures," *Comput. Phys. Commun.* **183**(10), 2233–2244 (2012).
30. F. T. Ulaby, *Fundamentals of Applied Electromagnetics*, 5th ed. (Pearson/PrenticeHall, 2007).
31. M. F. Modest, *Radiative Heat Transfer*, 3rd ed. (Academic, 2003).
32. D. Chubb, *Fundamentals of Thermophotovoltaic Energy Conversion* (Elsevier, 2007).
33. P. Bermel, J. Lee, J. D. Joannopoulos, I. Celanovic, and M. Soljacic, "Selective solar absorbers," *Annu. Rev. Heat Transfer* **15**(15), 231–254 (2012).

1. Introduction

Thermophotovoltaic (TPV) systems are a promising technology to convert thermal energy into electricity by means of a selective emitter and a photovoltaic cell (PVC). For certain applications, a selective absorber may be used as well. Heat sources for TPV systems range from chemical micro-combustors [1,2], furnaces [3], to concentrated solar energy [4–6]. For TPV systems, the spectral selectivity of the absorbers/emitters is critical for efficient energy conversion. Similarly, the angular performance of the absorbers/emitters directly impacts the overall system efficiency and power density for many TPV systems. Specifically, solar TPV (STPV) systems require both spectrally selective and wide angle absorbers/emitters, such as shown in Fig. 1(a).

In this system, a solar concentrator focuses radiation onto the selective absorber which converts the irradiation to heat while minimizing thermal emission loss. With increasing

levels of optical concentration, sunlight is delivered at increasing angles of incidence. Furthermore, actual optical concentrators typically deliver diffuse-like radiation to the absorber due to non-idealities and practical design considerations. Ideal solar absorbers, thus, possess large acceptance angles for absorption at wavelengths below a cut-off wavelength ($\lambda < \lambda_c$), while maintaining low hemispherical emissivity above the cut-off ($\lambda > \lambda_c$),

On the opposing side of the absorber is a selective emitter, which thermally emits the absorbed energy towards a PVC. By matching the spectrum of the emitter to the bandgap wavelength (λ_g) of a PVC, the amount of non-converted radiation by the PVC can be significantly reduced. To maximize the energy conversion efficiency and the power density of TPV systems, ideal emitters display high emissivity below λ_g while maintaining spectral selectivity at large angles.

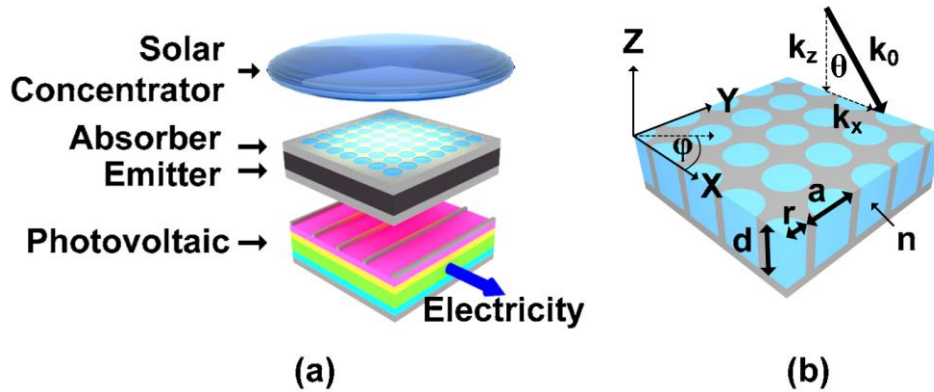


Fig. 1. (a) Schematic of a STPV system. (b) Schematic of the dielectric filled MPhC given the radius r , period a , depth d , index of cavity n , free-space wave vector k_0 , incident angle θ , and azimuthal angle ϕ .

Spectrally selective absorbers/emitters have been previously demonstrated via 1D [7], 2D [8–11], and 3D [12] metallic photonic crystals (MPhC). The 2D MPhC structure has shown great potential as selective absorbers/emitters due to its high temperature stability [13,14] and fabrication scalability [8].

However, traditional 2D MPhC radiation profiles are largely limited to a direction close to normal. Previously reported MPhCs show the radiation profiles falling from peak emissivity at approximately $\pm 30^\circ$ from normal incidence [8]. Such limited angular emission profiles negatively impact the overall efficiency and power density of TPV applications. Recent metamaterial based absorbers do show improved angular performance, however the narrow bandwidth of the previous designs severely impact the overall absorber/emitter power density in TPV systems [15–17]. Metamaterial designs based on metal dielectric stacks show wide angle and wide bandwidth performance [18–22], but are difficult to fabricate with high temperature compatible materials.

Our proposed dielectric filled 2D MPhC design, shown in Fig. 1(b), overcomes the narrow angular emission of previous designs, thus increasing the overall energy conversion efficiency and power density of TPV systems. Here, we present the theory and simulation results to demonstrate the improved angular performance of the dielectric filled MPhCs in comparison to air filled MPhCs. An efficiency comparison of the dielectric filled absorber and emitter MPhC in a STPV system is performed, which yields a 7% and 15.7% efficiency improvement relative to an air filled absorber and emitter MPhC design. Furthermore, we have previously reported using dielectric filled cavities to improve the thermal stability of silicon nanostructures as well as reduced cavity aspect ratios for ease of fabrication, thus revealing

other benefits of the dielectric filling [14,23]. The optical performance enhancements of dielectric filled metallic cavities are presented.

2. Theory

To improve the angular absorption/emission of the MPhC, we aim to reduce diffraction losses at oblique angles. To do so, the period of the MPhC needs to be reduced while keeping the cavity modes' wavelengths constant. We will see that this can be accomplished by adjusting the index n of the cavity. By using the diffraction grating equation, we calculate the minimum ratio λ/a required to avoid diffraction losses up to an incident angle of $\theta = 90^\circ$.

The selective absorption/emission of the MPhC is controlled by the cut-off wavelength of the cylindrical cavity modes. For incident light with free-space wavelength greater than the cut-off wavelength of the cavity ($\lambda > \lambda_c$), the incident light has no supported cavity mode to couple into, and the light is thus reflected. For incident light with free-space wavelength less than the cut-off wavelength of the cavity ($\lambda < \lambda_c$), the incident light couples into the cavity modes and thus absorption is enhanced due to the increased interaction time with the metallic walls. The cavity modes for a cylindrical waveguide with real metals, as shown in Fig. 1(b), can be analytically calculated by [24]

$$\lambda_{ij} = \frac{2\pi(r + \delta(\lambda_{ij}))n}{\chi'_{ij}} \quad (1)$$

where λ_{ij} is the free-space wavelength of the cavity mode (i, j), r is the radius of the cavity, $\delta(\lambda_{ij})$ is the skin depth as a function of wavelength, n is the index of the dielectric in the cavity, and χ'_{ij} is the j^{th} root of the derivative of the i^{th} Bessel function of the first kind (TE fundamental mode). For TM cavity modes χ'_{ij} can be replaced with χ_{ij} , the j^{th} root of the i^{th} Bessel function of the first kind. For typical TPV systems, the cut-off wavelength is usually set to the bandgap wavelength (λ_g) of the photovoltaic cell, and is thus a predefined constant. As a result, the cavity radius and index can be adjusted to match a particular cut-off wavelength. By choosing a cavity index $n > 1$, the radius of the cavity can be reduced by a factor proportional to n .

In order for incident light at oblique angles to efficiently couple into the cavity modes, diffraction losses must be minimized. Diffraction losses allow free-space radiation to reflect into undesired diffraction channels instead of coupling into the cavity modes [8,25, 26]. Such channels are undesired because, as previously discussed by Ghebrebrhan *et. al.*, diffraction destroys the Q-matching condition between the radiative Q_{rad} and the absorptive Q_{abs} of the cavity, thus reducing absorption. To analyze diffraction in the case of the MPhC grating structure, we begin with the grating equation

$$a(\sin \theta_i + \sin \theta_m) = m\lambda, m = \pm 1, \pm 2, \pm 3... \quad (2)$$

where a is the period, θ_i is the incident angle of the light, θ_m is the diffractive angle of order m , and λ is the free-space wavelength of light. The onset of diffraction at order m for normally incident light ($\theta_i = 0$) occurs when $\theta_m = 90^\circ$ which leads to $a = m\lambda$. For light at oblique angles, the onset of diffraction at order m occurs at

$$\theta_i = \sin^{-1} \left(\frac{\lambda m}{a} \mp 1 \right) \quad (3)$$

which is plotted in Fig. 2, with $m = 1$. The ∓ 1 indicates it is the opposite sign of m . Clearly, in Fig. 2, the larger the ratio of λ/a , the larger the value of θ_i . With a larger value of θ_i , larger incident angles of light may impinge on the MPhC without diffractive reflections. Thus to avoid diffraction at large incident angles for a constant λ , the period a must be reduced. In fact, the period need only be a factor of 2 ($\lambda/a = 2$) smaller than the free-space wavelength for θ_i to be 90° at the $m = 1$ mode (the cut-off mode). The expression in Eq. (3) is also used for calculating the angle and wavelength of Wood's anomaly, which will be discussed later in this paper [27].

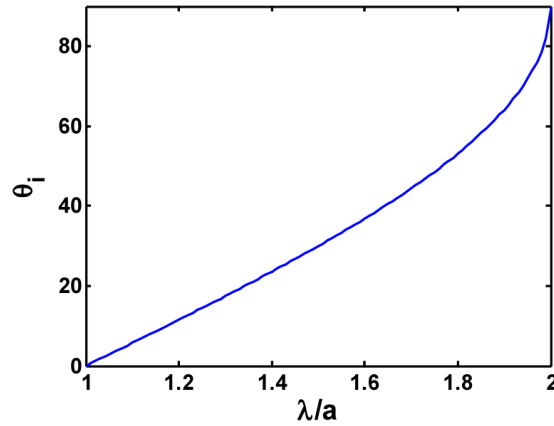


Fig. 2. The angle of incidence at the onset of diffraction of order $m = 1$ as a function of λ/a based on Eq. (3)

As previously discussed, for real TPV and STPV applications, the cutoff wavelength λ_c is usually determined by the bandgap wavelength of the PVC. Since the goal is to reduce the period a without changing the cut-off wavelength λ_c , the only solution based on Eq. (1) is to increase the index of the cavity n . For example, using Eq. (1) with an ideal metal where $\delta(\lambda_{i,j}) = 0$, with an air filled cavity of $n = 1$, radius $r = 586$ nm, period $a = 2r + 100$ nm, $\lambda_c = (\lambda_{1,1}) = 2 \mu\text{m}$, the ratio $\lambda_{1,1}/a = 1.57$ which yields a maximum incident angle of 34.8° . However, if the cavity is filled with a dielectric with $n = 1.3$, the radius reduced to $r = 450$ nm, $\lambda_{1,1} = 2 \mu\text{m}$, then the ratio $\lambda_{1,1}/a = 2$ which yields a maximum incident angle of 90° as shown in Fig. 2. Thus even a small increase in the cavity index from $n = 1$ to $n = 1.3$ can increase the incident angle from 34.8° to 90° without incurring diffraction losses, at the cut-off wavelength. To avoid diffraction losses for higher order modes, higher values of the cavity index will be needed.

The reasoning above explains the limited absorption/emission performance of previously published MPhC devices. For example in the MPhC design by Yeng *et. al.*, the ratio $\lambda/a = 1.53$, which leads to a maximum incident angle of 32° , which is in agreement with their simulated results [8]. The other previously cited works also used air filled cavities, and thus all suffer from the same angular emission profile [9–11,28].

3. Simulation results

3.1. Emissivity

The MPhC, as shown in Fig. 1(b), consists of an array of cylindrical holes in a metal substrate, with radius r , period a , and depth d . Simulations of both dielectric filled and air filled cavities are performed. Emission spectrums of the MPhC devices were computed with

the rigorous coupled wave analysis (RCWA) via the freely available software package S4 [29]. Simulated emission spectrums are taken from the simulated reflection spectrums R from an incident plane wave with electric field E_x , magnetic field H_y , and wavevector k_z . For opaque materials, the absorption A can be related to the reflection via $A=1-R$. The subsequent emission spectrum E can be related to the absorption via Kirchoff's law, where an object in thermal equilibrium emits as much radiation as is absorbed, or $E=A$. A complex permittivity model (Lorentz-Drude model) of tungsten is used in the simulations which is obtained from experimentally measured emittance of flat tungsten at room temperature [8]. Tungsten is chosen due to its high temperature stability and low emissivity at long wavelengths. The values of the cavity depths are determined via Q-matched conditions in order to maximize absorption [26]. The dielectric used in all subsequent simulations is an ideal dielectric with no losses and an effective index of $n = 1.8$, which corresponds to the index of hafnium oxide at a wavelength of 2 μm . For shorter wavelengths, the index increases, thus the chosen value is considered a lower limit. Hafnium oxide is chosen due to its ability to be deposit with the highly conformal atomic layer deposition (ALD) method, its transparent nature in the visible and infrared range (IR), and its high melting temperature.

The simulated emissivity spectrums at various incident angles are shown in Fig. 3, for both air filled cavities and dielectric filled cavities. All of the emissivity spectrums in Fig. 3 are averaged over both transverse electric (TE) (S-Polarized), and transverse magnetic (TM) (P-polarized), polarized light. The spectrums in Figs. 3(a) and 3(b) are averaged over the azimuthal angles from $\varphi = 0^\circ$ to $\varphi = 90^\circ$, which is equivalent to all azimuthal angles due to the radial symmetry of the MPhC structure. The spectrums in Figs. 3(c) and 3(d) are simulated at $\varphi = 0^\circ$.

In Fig. 3(a), the emissivity spectrum of air filled cavities decays quickly as a function of incident angle, as is consistent with literature [8]. As the incident angle is increased, diffractive losses are increased thus reducing the emissivity. In Fig. 3(b), the emissivity spectrum for dielectric filled cavities are shown to be more robust to changes in incident angles. Figures 3(c) and 3(d) show the contour plot of the emissivity as a function of the incident angle θ and free-space wavelength λ at $\varphi = 0^\circ$ of the air filled cavity in Fig. 3(c) and the dielectric filled cavity in Fig. 3(d). The diffraction thresholds for up to the first four orders from Eq. (3) are plotted in white. When the free-space wavelength of the two lowest order cavity modes are below the diffraction threshold in Fig. 3(c), the emissivity is reduced due to diffraction losses. However, in the dielectric filled cavities the reduced period causes the diffraction threshold to decrease in wavelength, and the diffraction losses are significantly reduced. Thus as predicted, the dielectric filled cavities have a more uniform emissivity profile and cut-off wavelength as a function of incident angle than the air filled cavity design.

The dielectric filled MPhC design is also robust to changes in azimuthal angle. The azimuthal angle φ impacts the emissivity spectrums since φ changes the effective period seen by in the incident light for nonzero incident angles θ . For example, a square array with period a , as defined in Fig. 1(b), will have an effective period of $a' = \sqrt{2}a$ at $\varphi = 45^\circ$. This effective increase in period will increase the diffraction threshold thus making the emissivity spectrum more sensitive to incident angle θ . The crossing of the cut-off wavelength with the $m = 1$ diffraction threshold line for the air filled MPhC design, from Fig. 3(a), will shift from $\theta = 35^\circ$ to $\theta = 6.4^\circ$ at $\varphi = 45^\circ$, thus causing diffraction losses at lower incident angles. Clearly, this change in emissivity will apply to all angles of $\varphi > 0^\circ$ for the air filled MPhC design. As a result, a difference in the air filled MPhC design is observed between the azimuthally averaged emissivity spectrum of Fig. 3(a) and the contour plot of Fig. 3(c) where $\varphi = 0^\circ$. However, for the dielectric filled MPhC design at $\varphi = 45^\circ$, the cut-off wavelength is still above the diffraction threshold for all θ , thus significantly reducing the impact of the azimuthal angle φ on the emissivity spectrum. Therefore, the emissivity spectrum of the dielectric filled MPhC is more robust to the azimuthal angle φ than the air filled MPhC design.

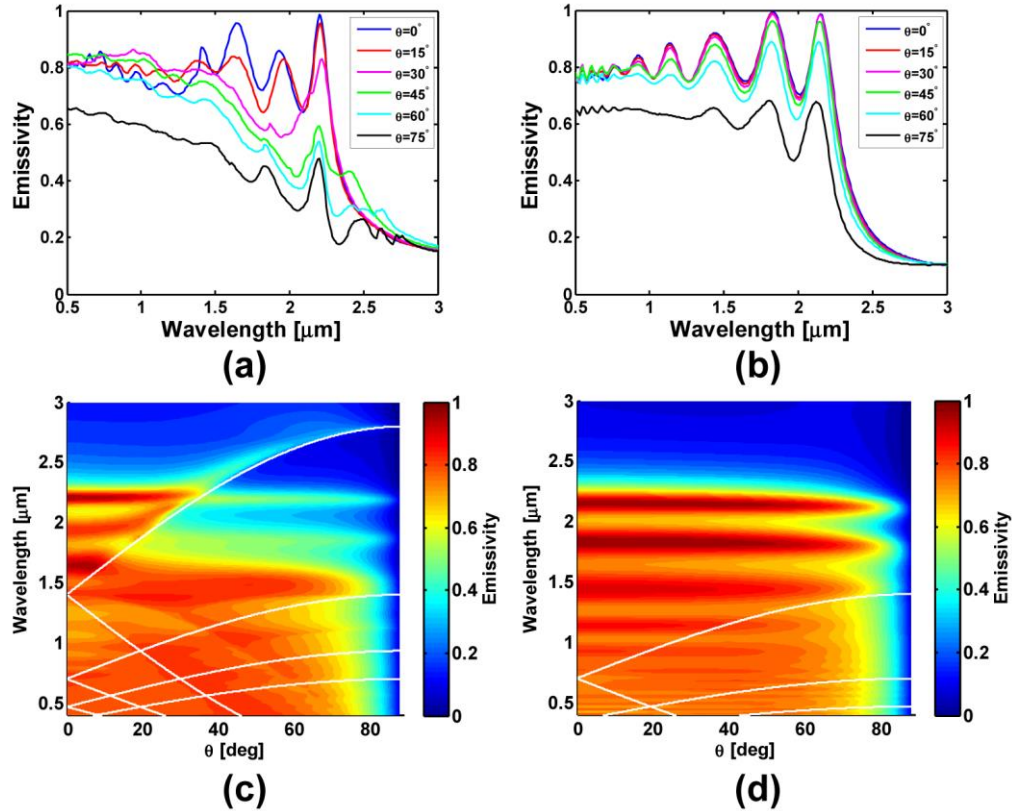


Fig. 3. Simulated emissivity spectra. (a) Shows the spectrum of an air filled ($n = 1$) cavity with dimensions $r = 0.625 \mu\text{m}$, $d = 2.8 \mu\text{m}$, $a = 1.4 \mu\text{m}$, as a function of incident angle θ where φ is averaged from $\varphi = 0^\circ$ - 90° . As the incident angle is increased, the emissivity drops significantly. (b) Shows the spectrum of a dielectric filled ($n = 1.8$) cavity with dimensions of $r = 0.3 \mu\text{m}$, $d = 1.2 \mu\text{m}$, $a = 0.7 \mu\text{m}$, with φ averaged over $\varphi = 0^\circ$ - 90° . As the incident angle is increased, the spectrum remains much more robust. Contour plots of the emissivity as a function of incident angle and wavelength are shown for the air filled cavity (c) and the dielectric filled cavity (d) both at $\varphi = 0^\circ$. The white lines are the diffraction thresholds as defined in Eq. (3).

3.2. Polarization dependence

At normal incidence, the dielectric filled cavity is polarization independent due to the circular symmetry of the cavities. However, as the incident angle is increased, the TM and TE polarized emissivity spectrums begin to diverge. In Fig. 4(a), the TM polarized emissivity spectrum generally increases as the incident angle is increased. The diffraction thresholds from Eq. (3) are plotted in white.

For wavelengths below the first order $m = 1$ diffraction line, the emissivity increases as the incident angle increases and peaks at around the Brewster angle of $\approx 70^\circ$. At the Brewster angle, TM incident light transmits through the dielectric with zero reflections. At these wavelengths, the MPhC is no longer seen as a homogeneous material by the incident light since the cavity diameters are on the same order as the wavelengths. Simulations not shown here, reveal the Brewster angle peaks shift in incident angle as a function of $\arctan(n)$, which is consistent with Brewster angle theory [30]. Distinct emissivity peaks are observed at the overlap of the Brewster angle and the cavity modes.

As a comparison, the TE polarized emissivity spectrums of dielectric filled cavities as a function of incident angle are shown in Fig. 4(b), where no Brewster angle effects are observed. As a result, the emissivity gradually decays as the incident angle is increased.

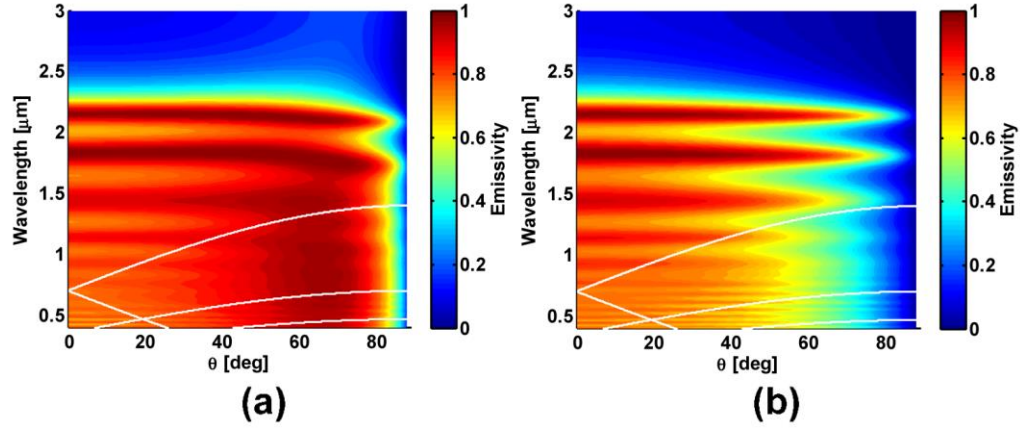


Fig. 4. Emissivity spectrum of dielectric filled cavities with (a) TM (P-Polarized) light versus (b) TE (S-Polarized) light as a function of incident angle θ and $\varphi = 0^\circ$. The dimensions of the cavities are the same as those in Fig. 3(b).

The emissivity spectrums of the air filled cavities are shown in Fig. 5(a) for TM and Fig. 5(b) for TE polarizations. Again the diffraction thresholds from Eq. (3) are plotted in white. The TM spectrum in Fig. 5(a) shows emission peaks above the cut-off wavelength at high incident angles, which is due to coupling into surface plasmon polariton (SPP) modes via Wood's anomaly at the diffraction order $m = 1$. Since Wood's anomaly only occurs for TM incident light, the emission peaks above cut-off are absent in the TE polarized spectrum in Fig. 5(b). Due to a lack of an air/dielectric boundary, no Brewster angle effects are observed in the TM case. High emissivity values are observed in the TM case for wavelengths less than $1.4 \mu\text{m}$ at incident angles up to 80° . Clearly the air filled cavities are more susceptible to non-ideal diffractive effects than the dielectric filled cavities.

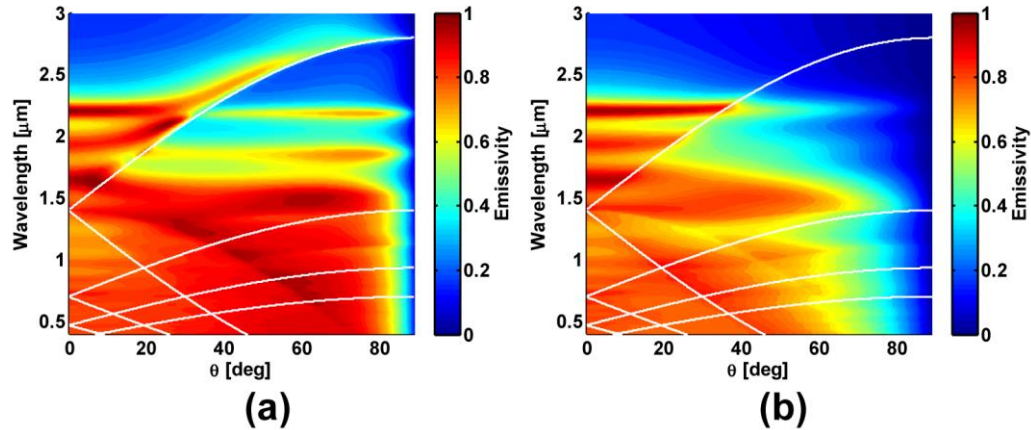


Fig. 5. Emissivity spectrum of air filled cavities with (a) TM (P-Polarized) light versus (b) TE (S-Polarized) light as a function of incident angle θ and $\varphi = 0^\circ$. Wood's anomaly can be observed in the TM spectrum but not the TE spectrum, as is consistent with theory. The dimension of the air filled cavities are the same as those shown in Fig. 3(a).

4. Analysis: dielectric filled absorbers/emitters for STPVs

The efficiency of STPVs relies on the performance of absorbers, for efficient collection of sunlight as heat, and the emitters, for efficient thermal emission at wavelengths below the bandgap wavelength (λ_g). To understand the impact of the dielectric filled cavities on the performance of STPV systems, a simulation comparing them to air filled cavities is performed. The emitter designs are the same as shown in Figs. 3(c) and 3(d). The absorber design uses a geometry designed for a cut-off of 1.75 μm for both the dielectric filled ($r=0.15\ \mu\text{m}$, $d=0.5\ \mu\text{m}$, and $a=0.35\ \mu\text{m}$) and air filled cavities ($r=0.4\ \mu\text{m}$, $d=1.1\ \mu\text{m}$, and $a=0.9\ \mu\text{m}$).

The performance for both cavity designs is evaluated based on the hemispherical emissivity which accounts for angularly-dependent properties and compared to the idealized performance assuming angularly-independent emissivity (computed at normal incidence). The hemispherical emissivities of the air filled cavities and dielectric filled cavities are calculated by Eq. (4) [31].

$$\epsilon_\lambda = \frac{1}{\pi} \int_0^\pi \int_0^{2\pi} \epsilon'_\lambda(\lambda, \varphi, \theta) \cos \theta \sin \theta d\varphi d\theta \quad (4)$$

Where ϵ_λ is the hemispherical emissivity at a particular wavelength λ , $\epsilon'_\lambda(\lambda, \varphi, \theta)$ is the emissivity as a function of λ , the polar angle θ , and the azimuthal angle φ , which is obtained from the RCWA simulations. Since black bodies are Lambertian, the emissivity observed along the hemisphere is the emissivity at each polar angle θ times the cosine of the polar angle θ .

To quantify the benefit of the dielectric filled MPhCs as absorbers, we evaluated the MPhCs based on the solar collection efficiency:

$$\eta_c = \bar{\alpha} - \frac{\bar{\epsilon}\sigma T^4}{CG_s} \quad (5)$$

where C is amount of optical concentration, G_s is the direct solar irradiance (900 W/m^2 for AM1.5D), $\bar{\alpha}$ is the solar-weighted absorptance, $\bar{\epsilon}$ is the emittance, σ is the Stefan-Boltzmann constant, and T is the temperature of the MPhC absorber. For both the normal and the hemispherical spectral properties, the dielectric filled MPhCs show higher solar collection efficiency compared to the air filled cavities, as shown in Table 1.

The performance of the emitters was evaluated based on the spectral efficiency which compares the amount of emission below the PVC bandgap ($\lambda < \lambda_g$) to the total amount of thermal emission (Q_e):

$$\eta_s = \frac{Q_{e,\lambda < \lambda_g}}{Q_e} \quad (6)$$

Because of the angular robustness of the dielectric filled cavities there is no degradation of the spectral efficiency between the normal and hemispherical emitter properties. In contrast, the emitter spectral efficiency of the air filled cavities is degraded by approximately 10%, as shown in Table 1. For a direct comparison of the dielectric filled cavities versus the air filled cavities, the hemispherical efficiencies of the absorber design and emitter design increased by 7% and 15.7%, respectively. These results demonstrate the importance of the angular robustness in terms of efficiency.

Table 1. Calculated STPV component efficiencies based on normal and hemispherical properties

	Dielectric filled cavity		Air filled cavity	
	Normal	Hemispherical	Normal	Hemispherical
Absorber - solar collection				
efficiency, η_c (%)	54.9	50.8	50.6	47.5
($250 \times$ - AM1.5D, $T = 1300$ K)				
Emitter - spectral efficiency of emission, η_s (%)	58.0	57.5	54.6	49.7
($T = 1300$ K, $\lambda_g = 2.22$ μm)				

Table 1 shows the benefits of the angular robustness of the dielectric filled cavities compared to the air filled cavities. For near-optimal performance [32], the temperature of the emitter (1300 K) was chosen such that the peak of Planck's blackbody distribution coincides with the PVC bandgap ($E_g = 0.556$ eV or $\lambda_g = 2.22$ μm). The absorber temperature was set to the emitter temperature. Given the absorber temperature, the amount of optical concentration ($C = 250$) was chosen such that the ideal cutoff wavelength approximately coincides with the design cutoff ($\lambda_c = 1.75$ μm) [33].

Another important metric for both TPV and STPV systems is the converted output power density of the PVC. The actual power conversion is also highly dependent on the angular absorption of the PVC. However, here we focus solely on the selective absorber/emitter comparing unfilled and filled MPhC designs, and hence we consider the output power density when the emitter is coupled to an idealized PVC ($E_g = 0.556$ eV or $\lambda_g = 2.22$ μm). The converted power density from the PVC is calculated by [32]

$$P_D = \pi \int_0^{\lambda_g} \epsilon_\lambda \frac{2hc^2}{\lambda^5} \frac{1}{e^{\left(\frac{hc}{\lambda k_B T}\right)} - 1} \frac{\lambda}{\lambda_g} d\lambda \quad (7)$$

where P_D is the converted power density, ϵ_λ is the hemispherical emissivity from Eq. (4), h is Planck's constant, c is the speed of light, λ is the wavelength of light, k_B is the Boltzmann constant, T is the temperature, and λ_g is the bandgap wavelength of the PVC [31]. The term λ / λ_g represents the fraction of the photon energy that can be utilized by the PVC, which is due to thermalization for photon wavelengths below the bandgap wavelength [22].

The calculated converted power densities for the dielectric filled and air filled MPhC designs are shown in Table 2. A converted power density increase of 33.5% is observed for the dielectric filled MPhC design. The large converted power density increase is due to the overlap of both the peak black body distribution and the peak of the λ / λ_g term with the cut-off wavelength (2.2 μm) of the emitter. With this specific configuration, the emissivity near the cut-off wavelength is heavily weighted when calculating the converted power density. Since the air filled MPhC emissivity near the cut-off wavelength is severely reduced for $\theta > 35^\circ$, as shown in Fig. 3(c), the overall converted power density is also severely suppressed. Whereas the dielectric filled MPhC emissivity near the cut-off wavelength, as shown in Fig. 3(d), remains high for large values of θ . Thus, we see angular robustness is also beneficial to the converted output power density.

Table 2. Calculated converted power densities

	Dielectric filled cavity <i>Hemispherical</i>	Air filled cavity <i>Hemispherical</i>	% change
PVC Converted Power Density, P_D ($T = 1300$ K, $\lambda_g = 2.22 \mu\text{m}$)	2.43 W/cm ²	1.82 W/cm ²	33.5%

Table 2 shows the increased converted power density from the PVC using the dielectric filled MPhC as compared to the air filled MPhC. The temperature of the emitter is again chosen to be 1300 K which corresponds to both the bandgap of the PVC ($E_g = 2.22 \text{ eV}$ or $\lambda_g = 2.22 \mu\text{m}$) and the cut-off wavelength of the emitter ($\lambda_c = 2.22 \mu\text{m}$).

5. Conclusion

We demonstrate the theory and simulation of the dielectric filled MPhC for wide angle absorption/emission properties for the application of TPV systems. We have shown that the dielectric in the cavities reduces the period of the MPhC while maintaining a constant cut-off wavelength λ_c , thus reducing undesired diffraction losses at oblique angles. By eliminating diffraction channels at oblique angles, the coupling of the incident light to the cavity modes is significantly increased. As a result, the absorption/emission of dielectric filled MPhC at oblique angles is significantly improved when compared to air filled cavities. We calculate that the minimum ratio of incident wavelength to period (λ/a) need only be a factor of 2 to avoid diffraction losses up to 90° for the cut-off wavelength. A STPV analysis using the dielectric filled cavities is performed, which shows a 7% and 15.7% improvement for the absorber and emitter efficiency, respectively, in comparison with the air filled cavities. The converted output power density is also increased by 33.5% for the dielectric filled MPhC design.

Acknowledgments

This material is based on the work supported as part of the Solid State Solar-Thermal Energy Conversion Center (S3TEC), an Energy Frontier Research Center funded by the U.S. Department of Energy, Office of Science, Office of Basic Energy Sciences under award DE-SC0001299/DE-FG02-09ER46577.